Research Article

Hydrothermal Synthesis of Iodine-Doped Bi$_2$WO$_6$ Nanoplates with Enhanced Visible and Ultraviolet-Induced Photocatalytic Activities

Jiang Zhang,[1] Zheng-Hong Huang,[1] Yong Xu,[2] and Feiyu Kang[1]

[1] *Laboratory of Advanced Materials, Department of Materials Science and Engineering, Tsinghua University, Beijing 100084, China*
[2] *Beijing Tongfang Puri-tech Co., Ltd, Beijing 100083, China*

Correspondence should be addressed to Zheng-Hong Huang, zhhuang@mail.tsinghua.edu.cn
and Feiyu Kang, fykang@mail.tsinghua.edu.cn

The iodine-doped Bi$_2$WO$_6$ (I-BWO) photocatalyst was prepared via a hydrothermal method using potassium iodide as the source of iodine. The samples were characterized by X-ray diffraction (XRD), scanning electron microscope (SEM), transmission electron microscopy (TEM) and selected area electron diffraction (SAED), X-ray photoelectron spectroscopy (XPS), UV-vis diffuse reflectance spectroscopy (DRS), and photoluminescence (PL) spectroscopy. The photocatalytic activity of I-BWO for the degradation of rhodamine B (RhB) was higher than that of pure BWO and I$_2$-BWO regardless of visible light (>420 nm) or ultraviolet light (<400 nm) irradiation. The results of DRS analysis showed that the I-BWO and I$_2$-BWO catalysts had narrower band gaps. XPS analysis proved that the multivalent iodine species including I^0 and I$^-$ were coadsorbed on the defect surface of Bi$_2$WO$_6$ in I-BWO. The enhanced PL intensity revealed that a large number of defects of oxygen vacancies were formed by the doping of iodine. The enhanced photocatalytic activity of I-BWO for degradation of RhB was caused by the synergetic effect of a small crystalline size, a narrow band gap, and plenty of oxygen vacancies.

1. Introduction

To decompose the organic pollutants existing in water and air, the advanced oxidation technique of photocatalysis was applied to deal with the serious environmental problems. Among all kinds of photocatalysts, the UV-induced TiO$_2$ as an effective photocatalyst have been applied widely in the conversion of photon energy into chemical energy and the decomposition of organic pollutants in air and water. For example, the photocatalytic technology had been used to disinfect water utilizing the solar energy [1]. In earlier researches, to develop visible-light-driven photocatalysts, in the case of TiO$_2$, the doping with nonmetal elements was regarded as a feasible modification to expand the photoresponsive range greatly and to inhibit the recombination of photoinduced electrons and holes efficiently [2–4]. In the past decades, the nitrogen-doped titanium dioxide was regarded as an effective case to improve the visible light photoresponsivity and to shift the optical absorption edge of TiO$_2$ towards a lower energy, thereby increasing the photoactivity. Among these nonmetal dopants, iodine-doping was paid more attentions owing to altering the surface charge, shifting the photoresponse from UV to visible region and acting as a conduction-band electron scavenger capable of inhibiting the rapid recombination of photoinduced electron-hole pairs [5–17].

Bi$_2$WO$_6$ is thought to be a promising visible-light-induced photocatalyst owing to its narrow band gap, presenting intrinsic photoabsorption and photoresponsivity from UV to visible light with wavelength of shorter than ca. 450–460 nm [18–22]. However, the photocatalytic efficiency of Bi$_2$WO$_6$ is very low owing to its drawbacks, such as limited visible light photoresponse, poor adsorption performance, poor dispersivity in water and high recombination opportunities of photoinduced electron-hole pairs. To improve the photoactivity of Bi$_2$WO$_6$, many efforts

on micro/nano-structures of Bi_2WO_6 had been made by solution self-assembly of nanoplates, such as hierarchical nest-like superstructure [20, 23] and hierarchical flower-like superstructure [24]. These superstructures with high surface area and porous structure are beneficial to the adsorption of organic molecules, improving the adsorption performance of Bi_2WO_6. In addition, the hollow structure of Bi-containing multimetal oxides [25, 26] has large specific surface area and special multiple scattering of UV-vis light within hollow frameworks, improving the visible light photocatalytic activity. It is well known that high photoinduced charge recombination is harmful to the photocatalytic activity of Bi_2WO_6. Therefore, it is necessary to take some measures to improve the migration efficiency of photoinduced electrons and suppress the recombination of photoinduced electrons and holes effectively. Recently, the modification of Bi_2WO_6 with Cu nanoparticles [27] exhibited a Fenton-like synergistic effect on improving the visible-light induced photocatalytic activity. Besides, Ag nanoparticles [28], C [29, 30], TiO_2 [31–33], $PtCl_4$ [34], Bi_2O_3 [35], Ag_2O [36], and $ZnWO_4$ [37] were also used to modify the Bi_2WO_6 catalyst, which can inhibit the recombination of photoinduced electrons and holes effectively and improve the photocatalytic performance greatly. The similar $BiVO_4$ modified $Bi_2O_2CO_3$ nanosheets hierarchical structure [38] exhibits an enhanced visible light photocatalytic activity. However, few studies have been focused on the UV-induced photocatalytic performance.

In the present study, the nonmetal element of iodine was used to modify the photophysical and photochemical performances of Bi_2WO_6. Herein, the iodine-doped Bi_2WO_6 nanoplates were synthesized by a hydrothermal process, and the photocatalytic activity was evaluated in terms of the decoloration of rhodamine B (RhB) under UV and visible light irradiation. The influences of iodine doping on the structure, optical properties, and morphologies of Bi_2WO_6 were investigated. And the corresponding mechanism of enhanced photocatalytic activity of I-BWO was also proposed in this work. In addition, I_2-loaded Bi_2WO_6 was also prepared to analyze the mechanism for higher photocatalytic activity of iodine-doped Bi_2WO_6 photocatalyst.

2. Experimental

2.1. Preparation of the Iodine-Doped Bi_2WO_6 Photocatalyst.
The iodine-doped Bi_2WO_6 catalyst was synthesized by a hydrothermal reaction. In a typical process, $Bi(NO_3)_3 \cdot 5H_2O$ (10 mmol) and Na_2WO_4 (5 mmol) were dissolved in 50 mL deionized water under magnetic stirring for 2 h to obtain a homogeneous white suspension. Subsequently, KI (1 mmol) was dissolved into the above suspension under magnetic stirring. Finally, the mixture was sealed into 100 mL Teflon autoclave and maintained at 160°C for 24 h. The as-obtained precipitate was filtrated, washed, and dried at 80°C for 5 h. The as-prepared iodine-doped Bi_2WO_6 was denoted as I-BWO. For comparison, the pure Bi_2WO_6 sample was also synthesized in the absence of iodine ions, and the corresponding catalyst was abbreviated as pure BWO.

In addition, I_2-loaded Bi_2WO_6 sample was also prepared by a simple method of impregnation as following: 16 mg I_2 was dissolved into 3 mL absolute ethanol. Subsequently, the above I_2-containing solution was dropped into 0.4 g pure BWO to form a mixed slurry by grinding in an agate mortar. Finally, the absolute ethanol was volatilized in the grinding procedure to obtain the dry powders, and this sample was marked as I_2-BWO.

2.2. Characterization of Photocatalysts.
The crystalline phases of the as-prepared catalysts were confirmed by powder X-ray diffraction (XRD). The XRD patterns of the samples were obtained by using a Rigaku Multiflex diffractometer at 40 kV and 200 mA with monochromated high-intensity Cu $K\alpha$ radiation. X-ray photoelectron spectra (XPS) were performed with a VG scientific ESCA Lab Mark II spectrometer which was equipped with a monochromatic Mg $K\alpha$ ($h\nu = 1253.6$ eV) excitation source. The binding energies obtained in the XPS spectral analysis were calibrated for specimen charging by referencing C 1s to 284.8 eV. The surface morphology of the as-synthesized samples was observed by a field emission scanning electron microscope (FE-SEM). High-resolution transmission electron microscopy (HRTEM) was performed to determine the microstructure of the samples on JEOL-2010F operated at 200 kV. To prepare the transmission electron microscopy (TEM) sample, a small amount of catalyst was ultrasonically dispersed in ethanol. A drop of such suspension was placed on a 200-mesh Cu grid with holey carbon film and dried completely in air. The UV-vis diffuse reflectance spectra (DRS) were acquired on a Shimadzu UV-2450 spectrophotometer with ISR-240A integrating sphere assembly in the range of 200–800 nm. $BaSO_4$ was used as a reflectance standard. The photoluminescence (PL) spectra of the samples were recorded with a fluorescence spectrophotometer F-4500 at the range of 400–700 nm.

2.3. Evaluation of Photocatalytic Properties.
Photocatalytic activities of the samples were evaluated by the photocatalytic degradation of rhodamine B (RhB). A 300 W Xe lamp was used as the light source with a 420 nm cutoff filter and an ultraviolet reflected filter (<400 nm) to provide visible and ultraviolet light irradiation, respectively. In the typical process, 0.05 g of photocatalyst was dispersed into a beaker, which was filled with 100 mL of 4×10^{-5} mol/L RhB solution. The as-obtained suspension was stirred for 2 h in the dark in order to establish the adsorption and desorption equilibrium between the photocatalyst and RhB. Then the suspension was irradiated under ultraviolet light (<400 nm) or visible light (>420 nm). At the given intervals, a 4 mL solution was sampled and centrifuged to remove the suspended solid photocatalyst. The concentration of RhB solution was determined by measuring the absorbance at the characteristic band of 553 nm using a Shimadzu UV-2450 spectrophotometer.

3. Results and Discussion

3.1. XRD Analysis.
The crystal phase compositions of as-prepared photocatalysts were characterized by the powder X-ray diffraction, and the corresponding XRD patterns of pure

BWO, I-BWO, and I_2-BWO samples are shown in **Figure 1**. All diffraction peaks of as-prepared samples appear to be in accordance with the standard orthorhombic phase of Bi_2WO_6 (JCPDS no. 39-0256). New crystal orientations or changes in preferential orientations are not observed in I-BWO and I_2-BWO comparing with pure BWO. This result indicates that the crystal phase of Bi_2WO_6 has not been influenced by the doping of I^- ions or the loading of I_2. In addition, the diffraction peaks of I-BWO and I_2-BWO are obviously weaker and broader, which indicate smaller crystalline sizes comparing with pure BWO. The average crystalline sizes calculated by the half-width of the maximum diffraction peak of the (131) crystallographic plane according to the scherrer equation for the pure BWO, I-BWO and I_2-BWO are 20.67 nm, 13.64 nm and 18.6 nm, respectively (listed in **Table 1**). It can be seen that compared with pure BWO, the crystalline sizes of I-BWO and I_2-BWO samples decrease. It is obvious that the crystallite growth can be inhibited by the iodine doping owing to the enhanced the energy barrier of mutual diffusion among the grains in the presence of potassium iodide caused by the repulsion among the adsorbed iodine species. However, the smaller crystalline size for I_2-BWO sample was caused by the small crystalline size of I_2. By careful comparison in **Figure 1(b)**, the diffracted intensity of the (131) crystallographic plane in the range of $2\theta = 26$–$30°$ decreases drastically as a result of doping with I^- ions. This indicates that the crystallinity of Bi_2WO_6 becomes lower with the introducing of iodine dopant. Moreover, the diffraction peak of the (131) crystallographic plane becomes much wider by the doping of I^- ions. **Table 1** compares the lattice parameters of pure BWO and I-BWO as determined by rietveld refinement of the relevant X-ray powder diffraction patterns. The lattice parameter along b-axis orientation increases owing to the doping of I^- ions.

3.2. Morphologies and Microstructures of Photocatalysts.

The typical scanning electron microscopy images of as-synthesized pure BWO, I-BWO, and I_2-BWO photocatalysts are shown in **Figure 2**. The pure BWO sample is composed of well-dispersed nanoplates, as shown in **Figure 2**. The edges of nanoplates are irregular and a slight aggregation is observed among the Bi_2WO_6 nanoplates. By contrast with pure Bi_2WO_6, the I-BWO sample is composed of sheet-like morphological nanoplates. As shown in **Figure 2**, the diameter of I-BWO nanoplates is smaller than that of pure BWO, and the dispersivity of nanoplates in I-BWO is better than that of pure BWO owing to the repulsion among the negatively charged iodine species adsorbed on the surface of nanoplates. However, the I_2-BWO sample is composed of the aggregated nanoplates and nanoparticles loading on the surface of Bi_2WO_6. It can be deduced that the nanoparticles are ascribed to I_2 loading on the Bi_2WO_6 nanoplates compared with the pure BWO sample. The rough surfaces of I_2-BWO are different from the smooth surfaces of pure BWO and I-BWO samples. The microstructure of the iodine-doped Bi_2WO_6 sample was investigated by TEM. **Figure 3(a)** shows the morphology of I-BWO synthesized by a hydrothermal reaction at 160°C for 24 h. The I-BWO sample is composed of two-dimensional nanoplates
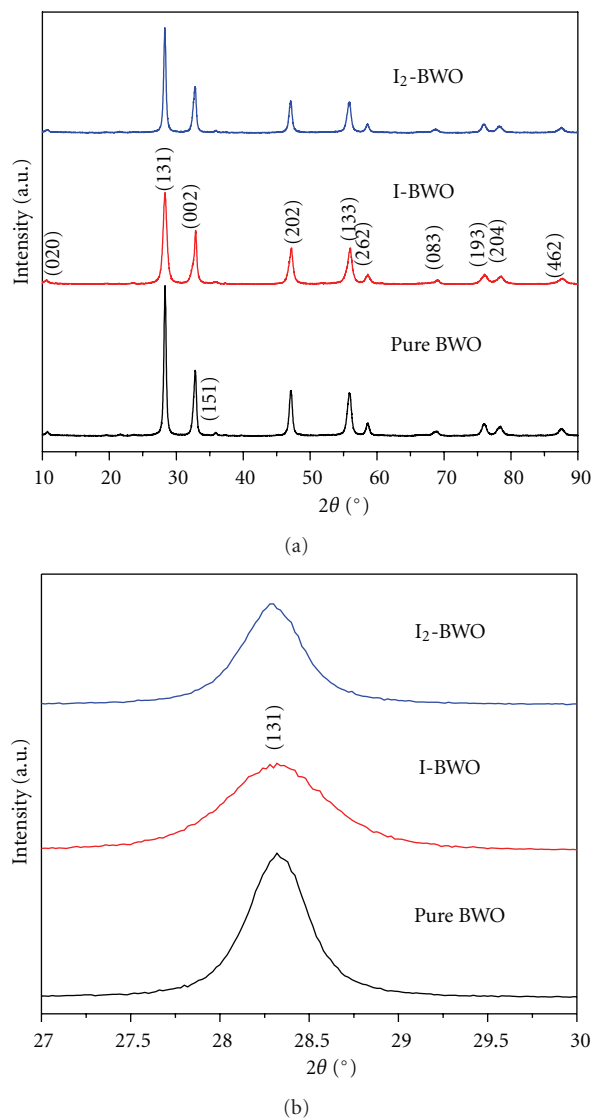

(a)

(b)

Figure 1: XRD patterns of the as-prepared pure BWO, I-BWO and I_2-BWO samples.

with the diameter of 50–100 nm. An HRTEM image of I-BWO is shown in **Figure 3(b)**. The distance between two planes in I-BWO is about 0.248 nm, which is similar to the d-spacing of (151) plane of orthorhombic Bi_2WO_6. The selective area electron diffraction (SAED) pattern of I-BWO sample in **Figure 3(c)** shows the irregular electron diffraction spots, highlighting the microcrystalline nature of the I-BWO sample. The different electron diffraction spots have been indexed by measuring the interplanar crystal spacings. The characteristic spots of the SAED pattern for I-BWO were assigned to the diffractions from the (131), (262), (174), (351), and (241) planes. The microcrystalline nature of I-BWO indicates that the I-BWO sample is a transient state from polycrystalline nature to monocrystalline nature.

To further confirm the composition of the iodine-doped Bi_2WO_6, the energy dispersive spectrum was measured to analyze the elements and contents of the as-prepared I-BWO.

TABLE 1: The average crystalline sizes and lattice parameters of the as-prepared samples.

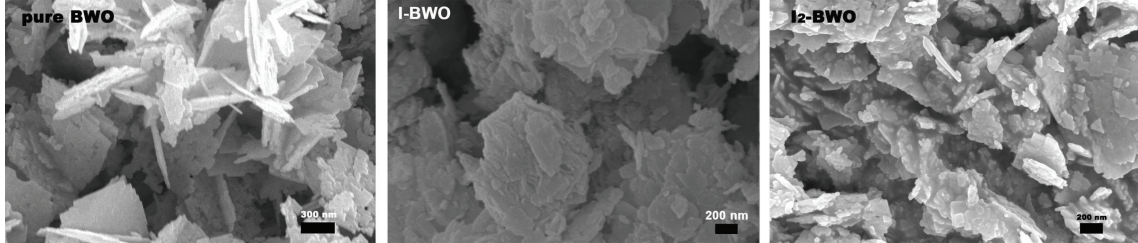| Sample	D (131)/nm	Lattice parameters		
		a/Å	b/Å	c/Å
Pure BWO	20.67	5.452	16.426	5.444
I-BWO	13.64	5.459	16.446	5.441
I_2-BWO	18.6	5.455	16.414	5.443

FIGURE 2: The typical SEM images of the as-prepared pure BWO, I-BWO and I_2-BWO samples.

Figure 4 shows that the main peaks of Bi, W, O, and Cu elements are exhibited in the spectrum of I-BWO, while the peak of iodine element is not observed owing to the trace doping of iodine. Herein, the peak of Cu element was ascribed to the background signal of Cu grid. There are several additional peaks of Cr, Re, Os, and Th species which are attributed to the instrumental error.

3.3. Optical Property.
The UV-visible diffuse reflectance spectra of pure BWO, I-BWO, and I_2-BWO samples are shown in Figure 5. The pure BWO sample exhibits the absorption edge around 440 nm. As shown in Figure 5(a), the I-BWO sample exhibits much stronger absorbance in the region of 200–450 nm comparing to pure BWO and its absorption band has an obvious red shift owing to the doping of I$^-$ ions. However, the enhanced absorption in the range from 440 to 700 nm are not observed, indicating that the doping of I$^-$ ions is formed by the surface adsorption instead of the lattice doping of Bi_2WO_6. The I_2-BWO sample has a larger red shift of absorption edge. By comparison, the I-BWO sample has a stronger ultraviolet light absorption than pure BWO and I_2-BWO. The steep shape of UV-vis diffuse spectra indicates that the absorption for visible light is not caused by the transition from the impurity level of I$^-$ ions but is induced by the intrinsic band gap transition of Bi_2WO_6. For a crystalline semiconductor, the optical absorption near the band edge could be estimated by the equation $ah\nu = A(h\nu - E_g)^{n/2}$, where a, ν, E_g, and A are absorption coefficient, light frequency, band gap, and a constant, respectively. Herein, the value of n for Bi_2WO_6 was 1. To estimate the band gap of samples, a modified plot of Kubelka-Munk function versus the energy of exciting light was shown in Figure 5(b). The band gap energy can be estimated from a plot of $(ah\nu)^{1/2}$ versus photon energy $(h\nu)$. The intercept of the tangent to the plot will give a good approximation of the band gap energy for indirect band gap materials. The estimated band gaps for pure BWO, I-BWO, and I_2-BWO from the intercepts of the tangents to the plots were 2.57, 2.48, and 2.33 eV, respectively. This result reveals that a narrower band gap is obtained by the iodine doping, indicating that the I-BWO sample possesses a suitable band gap for utilizing visible light and photocatalytic decomposition of organic contaminants under visible light irradiation. The I_2-BWO sample has a narrower band gap than I-BWO, improving the visible light absorption by I_2 loading.

3.4. XPS Analysis.
To analyze the surface compositions and chemical states of the as-prepared iodine-doped Bi_2WO_6 sample, X-ray photoelectron spectra were obtained as shown in Figure 6. The XPS measurement for I-BWO reveals the presence of Bi, W, O, I, and C elements. The binding energies given in the XPS analysis were calibrated for specimen charging by referencing C 1s to 284.80 eV. As shown in Figure 6, the high-resolution XPS spectra of the C 1s orbit has a peak at 284.8 eV. This was attributed to the surface amorphous carbon of the referenced C 1s from the XPS instrument itself. The O 1s core level spectrum of I-BWO could be fitted by the peak at binding energy of around 530.2 eV [34] in Figure 6, indicating that the oxygen species are assigned to the lattice oxygen ions and hydroxyl oxygen on the surface [39]. The high-resolution XPS spectrum of I 3d5 core level on the surface of I-BWO is shown in Figure 6. The I 3d5 core level spectrum of I-BWO was composed of two peaks at 632.0 eV and 619.4 eV, which were ascribed to I $3d_{3/2}$ and I $3d_{5/2}$, respectively, which were different from the binding energies of 630.1 and 618.3 eV relating to the characteristic bands of iodine in I_2 [40]. Herein, the peak at 619.4 eV should be ascribed to the negatively charged iodine (I$^-$) species, while the other peak at 632.0 eV can be attributed to I_2 (631.0 eV). The chemical shift of 1.0 eV was caused by the surface adsorption of Bi_2WO_6 for I_2. It is probable that the I$^-$ ions may undergo the following chemical reaction to form I_2 during the hydrothermal process: $4I^- + O_2 + 4H^+ \rightarrow 2I_2 + 2H_2O$. The trace amount of iodine dopant was measured in I-BWO by the elementary
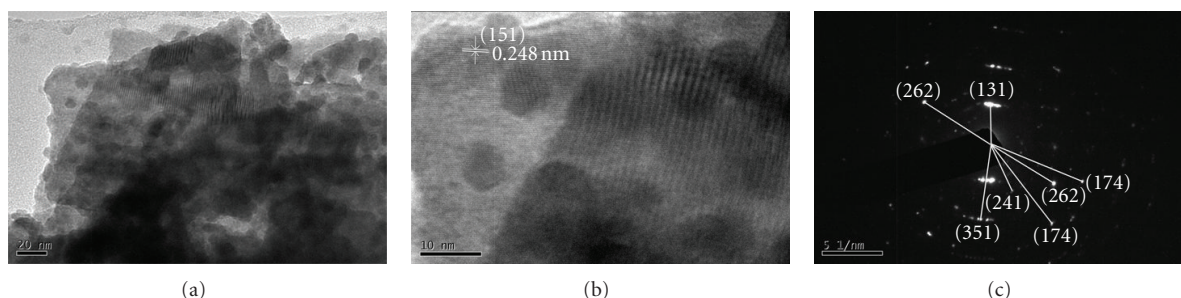
Figure 3: (a) TEM microphotograph of the iodine-doped Bi_2WO_6 (I-BWO); (b) high-resolution TEM photograph of I-BWO; (c) SEAD pattern of I-BWO.
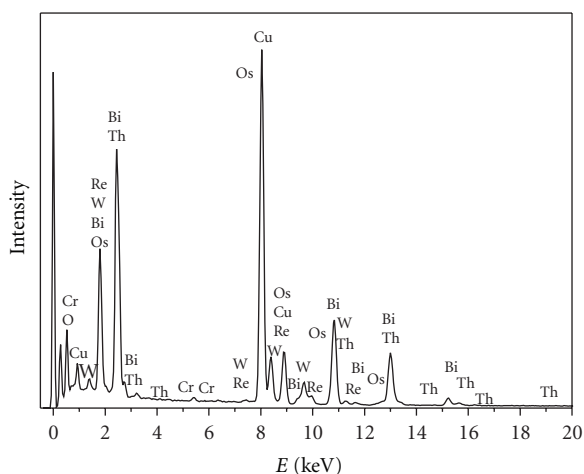

Figure 4: Energy dispersive spectrum for the as-prepared I-BWO.

analysis, and the atomic content of iodine dopant was 0.31%. Since the ionic radius of I^- (0.216 nm) is much larger than that of O^{2-} (0.124 nm), the substitution of O^{2-} ions in the lattice by I^- would occur difficultly. Thus I_2 and I^- species were probably adsorbed on the surface defect sites of Bi_2WO_6 nanoplates, since the position of the diffraction peaks of I-BWO are exactly the same as that of pure BWO. To determine the oxidation state of Bi, the Bi 4f XPS peak for sample I-BWO was shown in Figure 6. The characteristic spin-orbit split of Bi $4f_{5/2}$ and Bi $4f_{7/2}$ signals [41–43] at approximately 164.4 eV and 159.2 eV in I-BWO sample demonstrates that the main chemical state of bismuth in the iodine-doped sample was trivalence (Bi^{3+}), which is similar to the reported values of pure Bi_2WO_6 [44, 45]. The XPS spectrum of W 4f (Figure 6) in I-BWO shows a resolved doublet due to the tungsten W $4f_{5/2}$ and W $4f_{7/2}$ components observed at binding energies of 37.4 eV and 35.4 eV, respectively. The difference in binding energy of the resolved doublet is 2.0 eV, corresponding to the W^{6+} oxidation state. An additional resolved doublet due to the tungsten W $4f_{5/2}$ and W $4f_{7/2}$ components is observed at binding energies of 29.2 eV and 26.2 eV, respectively. The difference in binding energy of the resolved doublet is 3.0 eV, corresponding to the W^{4+} oxidation state [23, 46]. The appearance of W^{4+} valence

indicates that a lower oxidation state of tungsten element is formed by the doping of iodine. It is possible that the coordination environment of tungsten was changed owing to the coadsorption of I^- and I_2 species on the surface defect sites of sheet-like Bi_2WO_6 nanoplates.

3.5. Photocatalytic Activity for RhB under Ultraviolet and Visible Light Irradiation. After the dark adsorption, the RhB adsorption of pure BWO is only 3.5%, while that of I-BWO is up to 16%. In addition, the RhB adsorption of I_2-BWO is similar to pure BWO. Therefore, the I-BWO sample displays a higher adsorption capability for RhB than that of pure BWO and I_2-BWO. Then the photocatalytic activities of the as-prepared samples were evaluated by the degradation of RhB under ultraviolet (<400 nm) or visible light (>420 nm) irradiation. As can be seen in Figure 7, the I-BWO sample displays a higher photocatalytic activity than that of pure BWO and I_2-BWO under ultraviolet light or visible light irradiation. The photodegradation efficiencies of RhB over pure BWO, I-BWO, and I_2-BWO samples are up to 49%, 80%, and 84% after 120 minutes visible light irradiation, respectively. However, the corresponding UV-induced photodegradation efficiencies of RhB are up to 35%, 85%, and 58%, respectively. The photodegradation efficiency of RhB for I_2-BWO under visible light irradiation is slightly higher than that for I-BWO, which is caused by a lower amount of RhB owing to the strong adsorption of I-BWO for RhB. This result proved that the enhanced visible-light-induced and ultraviolet-light-induced photocatalytic activities were obtained by the doping of iodine. Furthermore, it is found that the photocatalytic activities of all photocatalysts induced by ultraviolet light are higher than that induced by visible light. To obtain the same removal rate for RhB, the visible-light-induced photodecomposition process would take much more time than the ultraviolet-light-induced photodecomposition process. As shown in Figure 7, the doping of I^- ions is more efficient to improve the photocatalytic activity of Bi_2WO_6 than the loading of I_2. The visible-light-induced photocatalytic activity of I-BWO sample is similar to that of I_2-BWO, while the UV-induced photocatalytic activity of I-BWO sample is greatly higher than that of I_2-BWO sample. The photodegradation
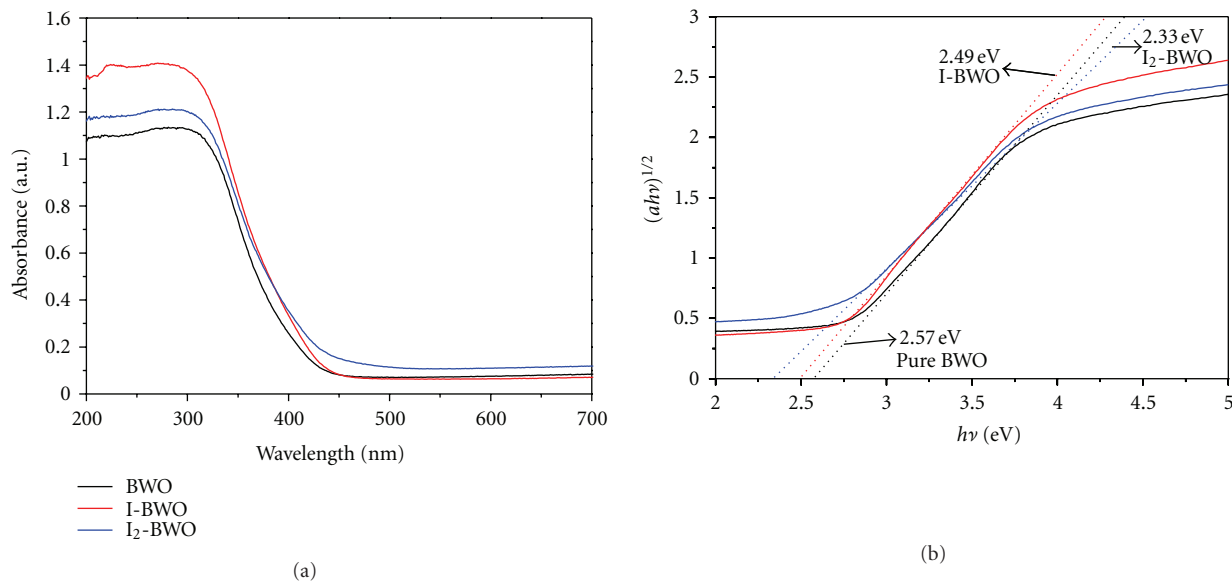
(a)

(b)

Figure 5: (a) UV-vis diffuse reflectance spectra for pure BWO, I-BWO, and I_2-BWO samples. (b) The relationship between $(ah\nu)^{1/2}$ and photon energy.

Table 2: The values of the photodegradation rate constant k for RhB and linearly dependent coefficient R^2.

Sample	Ultraviolet light		Visible light	
	k (mol L^{-1} min^{-1})	R^2	k (mol L^{-1} min^{-1})	R^2
Pure BWO	6.27×10^{-3}	0.929	5.97×10^{-3}	0.931
I-BWO	6.30×10^{-2}	0.947	4.03×10^{-2}	0.962
I_2-BWO	1.39×10^{-2}	0.994	1.72×10^{-2}	0.987

efficiency of I-BWO is 1.47 times larger than that of I_2-BWO. These results revealed that as-prepared catalysts were regarded as bifunctional photocatalysts, exhibiting excellent photocatalytic performances under ultraviolet and visible light irradiation.

To distinguish the photocatalytic activities of the as-prepared samples, the kinetic fitted curve plots for photodegradation of RhB under different light source with various wavelength ranges are shown in Figure 8. The corresponding values of the photodegradation rate constant k for RhB and linearly dependent coefficient R^2 were listed in Table 2. The value of $-Ln(C_t/C_0)$ increased linearly with time, indicating that the photodegradation of RhB under both ultraviolet and visible light irradiation over the as-prepared samples could be described as first-order reaction [47]. The photocatalytic activities of as-prepared samples can be evaluated by the values of k, that is, the higher the value of k is, the higher the photocatalytic activity is [48]. Moreover, the larger the coefficient R^2 is, the better the linear dependence relation is. As shown in Table 2, under UV illumination, the order of the values of k was 6.27×10^{-3} < 1.39×10^{-2} < 6.30×10^{-2}, corresponding to the slopes of kinetic fitted curves of pure BWO, I_2-BWO, and I-BWO, respectively. The photodegradation rate of I-BWO is 4.53 times larger than that of I_2-BWO under UV

irradiation. For comparison, under visible light irradiation, the order of the values of k was 5.97×10^{-3} < 1.72×10^{-2} < 4.03×10^{-2}, corresponding to the slopes of kinetic fitted curves of pure BWO, I_2-BWO and I-BWO, respectively. The photodegradation rate of I-BWO is 2.34 times larger than that of I_2-BWO under visible light irradiation. As above-mentioned, the photodegradation rate for RhB under ultraviolet light irradiation was higher than that under visible light irradiation in cases of I-BWO and pure BWO. However, the photodegradation rate for RhB under ultraviolet light irradiation is lower than that under visible light irradiation in case of I_2-BWO. Moreover, the photodegradation rates of the I-BWO and I_2-BWO for RhB are higher than that of pure Bi_2WO_6, regardless of ultraviolet or visible light irradiation. It can be deduced that during the photocatalytic reaction, I^0 acted as an electron acceptor and was reduced to I^-, and I^- was also oxidized to I^0 by photoinduced holes. Hence, an efficient separation of electron-hole pairs was obtained by surface iodine species containing I^0 and I^-. Thus, it is reasonable that I-BWO shows a higher photocatalytic activity than pure BWO. Different from I-BWO, the improved photocatalytic activity of I_2-BWO was obtained by the role of electron acceptor of I_2. In addition, the values of R^2 for visible-light-induced photocatalysis are higher than that for ultraviolet-light-induced photocatalysis in cases of pure
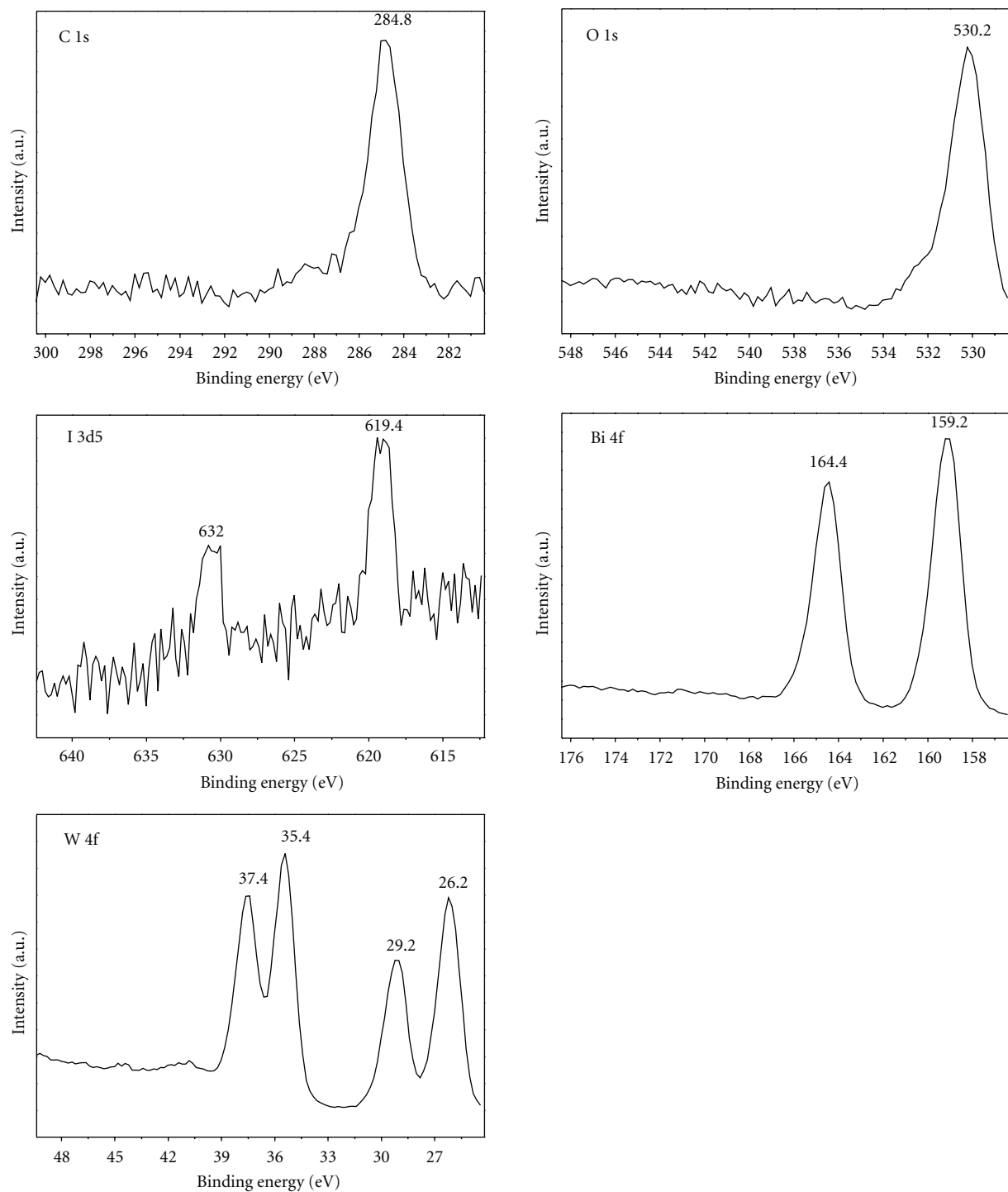
Figure 6: High-resolution XPS spectra analysis of C 1s, O 1s, I 3d5, Bi 4f, and W 4f.

BWO and I-BWO. This result proved that the linear dependence relation of visible-light-induced photocatalysis was better than that of ultraviolet-light-induced photocatalysis. And the visible-light-induced photodegradation for RhB using the as-prepared photocatalysts was even more similar to the first-order reaction.

3.6. Mechanism Discussion. The photoluminescence (PL) spectroscope, as one of the most powerful tools, has been utilized to investigate the carrier transfer, energy transportation, and energy conversion during the photochemical and photophysical processes. According to the results of Wen's group [49], the emission of fluorescence is related to the surface
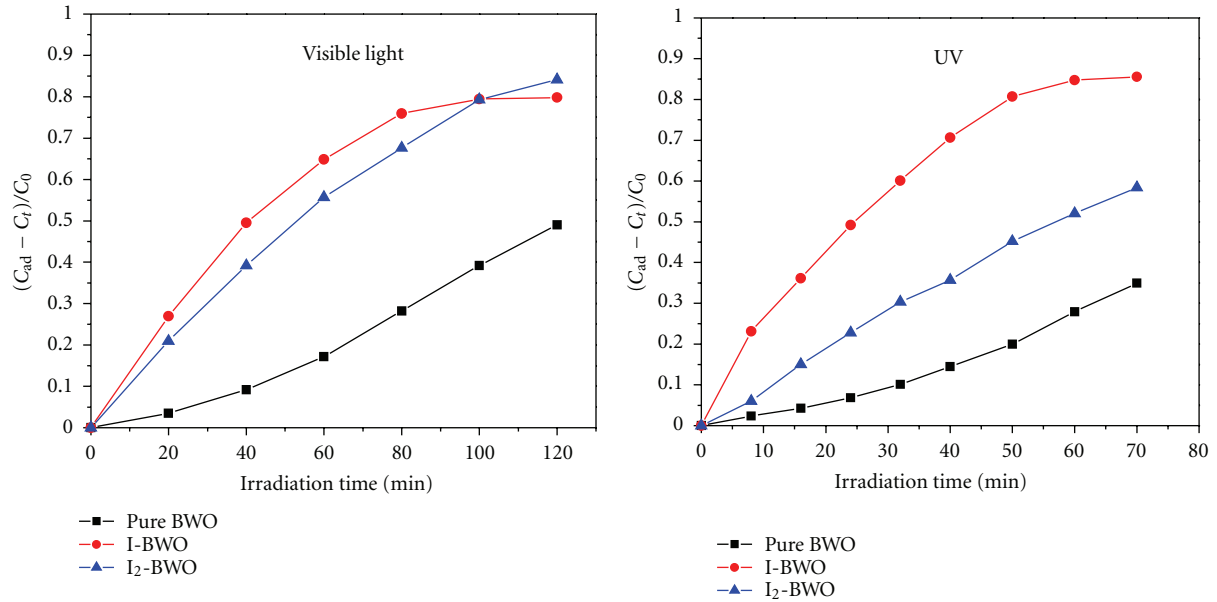
FIGURE 7: Photocatalytic activity for decomposition of rhodamine B (4×10^{-5} mol L^{-1}) under visible light (>420 nm) and ultraviolet light (<400 nm) irradiation at room temperature in air using pure BWO, I-BWO, and I$_2$-BWO as photocatalysts. C_{ad}: the concentration of RhB after dark adsorption, C_t: the concentration of RhB during the photocatalytic reaction, and C_0: the initial concentration of RhB before dark adsorption.
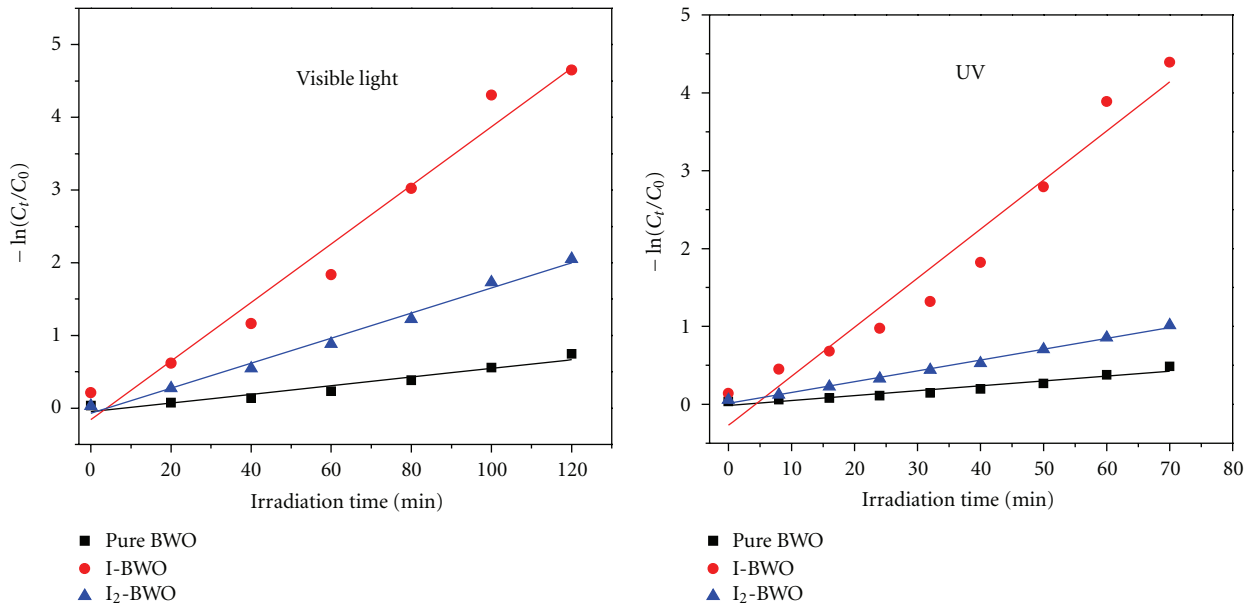

FIGURE 8: Kinetic fitted curve plots of photocatalytic degradation of RhB (4×10^{-5} mol L^{-1}) under visible light (>420 nm) and ultraviolet light (<400 nm) irradiation at room temperature in air over the as-prepared photocatalysts.

states or the density of defects. And the PL intensity originates from the number of recombination of the photoexcited electron-hole pairs; low intensity of fluorescence means a low recombination rate for the photoexcited electrons and holes. Figure 9 exhibits the PL spectra of pure BWO and I-BWO excited at different wavelengths. Figure 9(a) shows the PL spectra of the as-prepared samples excited by light with a wavelength of 338 nm in UV region. An obvious

visible band is obtained in the range of 430–520 nm, which is ascribed to a broad blue-green emission. The iodine-doped Bi$_2$WO$_6$ sample displays a large enhancement in the visible luminescence. And the PL intensity of I-BWO is greatly higher than that of pure BWO, indicating that the PL enhancement effect is caused by the doping of iodine species. However, the positions of PL peaks do not shift and there is no new PL peaks observed owing to the introduction
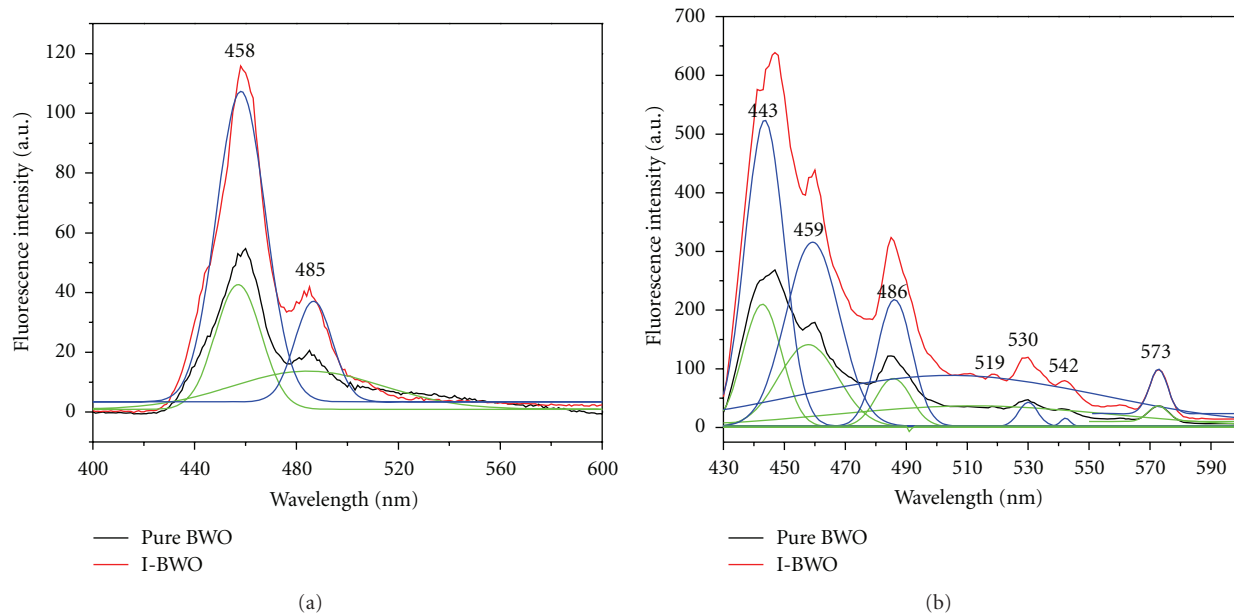
FIGURE 9: The room temperature Photoluminescence spectra of pure BWO and I-BWO (a) monitored at 338 nm, (b) monitored at 420 nm.

of iodine dopant. The visible band can be easily fitted with two broad Gaussian bands (Figure 9(a)), located in the blue (2.82–2.64 eV; 440–470 nm) and in the blue-green parts of the visible spectrum (2.70–2.38 eV; 460–520 nm) [14]. The strongest blue-emitting peaks at 458 nm were attributed to the intrinsic blue luminescence of Bi_2WO_6, which originates from the charge-transfer transitions between the hybrid orbital of Bi 6s and O 2p(VB) and the empty W 5d orbital (CB) in the $[WO_6]^{2-}$ complex. In addition, this emission peak reveals the spectral dependence of the intrinsic band-edge absorption for Bi_2WO_6. The redundant emitting peak at 485 nm (green) is ascribed to the defects of metal atoms and oxygen vacancies during the crystal growth process, which will become many defect centers, and thus affect the optical properties of Bi_2WO_6 [8]. For comparison, Figure 9(b) shows the PL spectra of the as-prepared samples excited by light with a wavelength of 420 nm in visible light region. Different from the situation of UV-excitation, there are several additional visible Gaussian bands around 443, 519, 530, 542, and 573 nm besides the above-mentioned two visible bands around 459 and 486 nm. The strong blue emission band centered at 443 nm is attributed to the intrinsic transition of Bi^{3+} ions from the 3P1 (6s6p) excited state to the 1S0 (6S2) ground state. The four visible bands around 519, 530, 542, and 573 nm are ascribed to the defects of oxygen vacancies caused by the doping of iodine. The enhanced visible PL intensity is also observed in the situation of visible light excitation in I-BWO. From the results of XRD, I-BWO possesses a smaller crystallite size than pure BWO, indicating a higher density of surface defects or oxygen vacancies. In the case of light excitation, the transition of photoinduced electrons increased with the increasing light absorption caused by surface defect, resulting in the enhancement of responding PL intensity [49].

According to the previous theoretical calculations [50], the coadsorption of I^- and IO_4^- ions on the defect surface of TiO_2 would result in the formation of new energy bands between the conduction band bottom and the valence band top of TiO_2. In the same way, the new energy bands was also introduced into the energy band structure of Bi_2WO_6 by the coadsorption of I^0 and I^- ions on the defect surface of Bi_2WO_6. The redox potential $E^0(I^0/I^-)$ = 0.54 V lies between the conduction band E_{cb} (Bi_2WO_6) = 0.46 V and the valence band E_{vb} (Bi_2WO_6) = 3.26 V [51]; hence the excitation of an electron from the valence band of Bi_2WO_6 to the surface adsorbed I^0 is qualified as practical. The photoinduced electrons are captured by the surface I^0 to produce I^-, while the holes left on the valence band of Bi_2WO_6 can induce the production of hydroxyl radicals (•OH) and further degrade the organic pollutants. In addition, the photocatalytic activity of I-BWO is higher than I_2-BWO. This indicates that the photoinduced electron is also utilized to accelerate the photodegradation of RhB via the capture of hole by surface I^- ions. Based on the results of XRD analysis, the crystallinity of the I-BWO was lower than that of pure BWO, which was not beneficial to improving the photocatalytic activity. However, it was found that the photocatalytic activity of I-BWO was higher than that of pure BWO. Therefore, we deduced that the crystallinity was not the decisive factor controlling photocatalytic activity. According to the results of UV-vis absorption spectra, a slight red shift of absorption spectrum for I-BWO was caused by the doping of I^- ions. The band gap estimated from absorption spectrum for I-BWO is slightly lower than that of pure BWO, indicating that the energy band structure becomes narrower by the doping of iodine. Although the light absorption had never been improved greatly, the doping of iodine resulted in the formation of an

impurity energy level at the bottom of conduction band of Bi_2WO_6. The narrowing band gap of I-BWO was beneficial to increasing the transfer rate of electrons to the photocatalyst surface, improving the separation efficiency of photoinduced electrons and holes. The small crystalline size of I-BWO is beneficial to the fast transfer of photoinduced electrons, improving the photocatalytic activity for the degradation of RhB. By comparison with I_2-BWO, the photoinduced electrons and holes are utilized efficiently to improve the photocatalytic activity of I-BWO. In the XPS analysis, the appearance of W^{4+} was caused by the lattice distortion of Bi_2WO_6 crystal owing to the surface adsorbed I^- species, resulting in the rearrangement of the internal electric field of Bi_2WO_6. In addition, the enhanced PL intensity of I-BWO proved the existence of defects of oxygen vacancies due to the doping of iodine, facilitating the effective separation of photoinduced electrons and holes and even enhancing the photocatalytic activity for the degradation of RhB.

4. Conclusion

The iodine-dope Bi_2WO_6 nanopaltes were synthesized via a hydrothermal process. The band gaps of I-BWO and I_2-BWO were narrower than that of pure BWO, resulting in the enhanced photoabsorption and photoresponsivity for visible light, increasing the number of photoinduced electron-hole pairs. The defects of oxygen vacancies caused by the doping of iodine were proved to be responsible for the enhanced PL intensity. As shown in XPS analysis, the multivalency iodine species including I^0 and I^- were coadsorbed on the defect surface of Bi_2WO_6. I^0 can be regarded as the acceptor of photoinduced electrons, while I^- can act as the acceptor of photoinduced holes. Hence, I-BWO exhibits more effective separation of the photoinduced electron-hole pairs than I_2-BWO. The as-prepared I-BWO exhibited the highest photocatalytic activities for photodegradation of RhB regardless of UV or visible light irradiation. The above-mentioned factors were responsible for the enhanced photocatalytic activity during the photodegradation of RhB. Moreover, the UV-induced photocatalytic activity was much higher than the visible-induced photoactivity. The iodine-doped Bi_2WO_6 could be regarded as a bifuncitonal photocatalyst to deal with the pollutants existing in water and air.

Acknowledgment

References

[1] J. A. Byrne, P. A. Fernandez-Ibañez, P. S. M. Dunlop, D. M. A. Alrousan, and J. W. J. Hamilton, "Photocatalytic enhancement for solar disinfection of water: a review," *International Journal of Photoenergy*, vol. 2011, Article ID 798051, 12 pages, 2011.

[2] R. Kun, S. Tarján, A. Oszkó et al., "Preparation and characterization of mesoporous N-doped and sulfuric acid treated anatase TiO_2 catalysts and their photocatalytic activity under UV and Vis illumination," *Journal of Solid State Chemistry*, vol. 182, no. 11, pp. 3076–3084, 2009.

[3] G. Liu, X. Wang, L. Wang et al., "Drastically enhanced photocatalytic activity in nitrogen doped mesoporous TiO_2 with abundant surface states," *Journal of Colloid and Interface Science*, vol. 334, no. 2, pp. 171–175, 2009.

[4] J. Yu, M. Jaroniec, and G. Lu, "TiO_2 photocatalytic materials," *International Journal of Photoenergy*, vol. 2012, Article ID 206183, 5 pages, 2012.

[5] Y. Ma, J. W. Fu, X. Tao, X. Li, and J. F. Chen, "Low temperature synthesis of iodine-doped TiO_2 nanocrystallites with enhanced visible-induced photocatalytic activity," *Applied Surface Science*, vol. 257, no. 11, pp. 5046–5051, 2011.

[6] Z. He, L. Zhan, F. Hong et al., "A visible light-responsive iodine-doped titanium dioxide nanosphere," *Journal of Environmental Sciences*, vol. 23, no. 1, pp. 166–170, 2011.

[7] R. Long, Y. Dai, and B. Huang, "Structural and electronic properties of iodine-doped anatase and rutile TiO_2," *Computational Materials Science*, vol. 45, no. 2, pp. 223–228, 2009.

[8] C. Wen, L. Sun, J. M. Zhang, H. Deng, and P. Wang, "Effect of iodine-doping on photocatalytic activity of TiO_2 photocatalyst," *Chemical Journal of Chinese Universities*, vol. 27, no. 12, pp. 2408–2410, 2006.

[9] W. Su, Y. Zhang, Z. Li et al., "Multivalency iodine doped TiO_2: preparation, characterization, theoretical studies, and visible-light photocatalysis," *Langmuir*, vol. 24, no. 7, pp. 3422–3428, 2008.

[10] S. Tojo, T. Tachikawa, M. Fujitsuka, and T. Majima, "Iodine-doped TiO_2 photocatalysts: correlation between band structure and mechanism," *Journal of Physical Chemistry C*, vol. 112, no. 38, pp. 14948–14954, 2008.

[11] G. Liu, C. Sun, X. Yan et al., "Iodine doped anatase TiO_2 photocatalyst with ultra-long visible light response: correlation between geometric/electronic structures and mechanisms," *Journal of Materials Chemistry*, vol. 19, no. 18, pp. 2822–2829, 2009.

[12] Y. Su, Y. Xiao, X. Fu, Y. Deng, and F. Zhang, "Photocatalytic properties and electronic structures of iodine-doped TiO_2 nanotubes," *Materials Research Bulletin*, vol. 44, no. 12, pp. 2169–2173, 2009.

[13] Z. He, L. Xie, J. Tu et al., "Visible light-induced degradation of phenol over iodine-doped titanium dioxide modified with platinum: role of platinum and the reaction mechanism," *Journal of Physical Chemistry C*, vol. 114, no. 1, pp. 526–532, 2010.

[14] F. Barka-Bouaifel, B. Sieber, N. Bezzi et al., "Synthesis and photocatalytic activity of iodine-doped ZnO nanoflowers," *Journal of Materials Chemistry*, vol. 21, no. 29, pp. 10982–10989, 2011.

[15] Q. Hou, Y. Zheng, J. F. Chen, W. Zhou, J. Deng, and X. Tao, "Visible-light-response iodine-doped titanium dioxide nanocrystals for dye-sensitized solar cells," *Journal of Materials Chemistry*, vol. 21, no. 11, pp. 3877–3883, 2011.

[16] Y. Z. Zheng, X. Tao, Q. Hou, D. T. Wang, W. L. Zhou, and J. F. Chen, "Iodine-doped ZnO nanocrystalline aggregates for improved dye-sensitized solar cells," *Chemistry of Materials*, vol. 23, no. 1, pp. 3–5, 2011.

[17] W. A. Wang, Q. Shi, Y. P. Wang, J. L. Cao, G. Q. Liu, and P. Y. Peng, "Preparation and characterization of iodine-doped mesoporous TiO_2 by hydrothermal method," *Applied Surface Science*, vol. 257, no. 8, pp. 3688–3696, 2011.

[18] Z. Zhang, W. Wang, J. Xu, M. Shang, J. Ren, and S. Sun, "Enhanced photocatalytic activity of Bi_2WO_6 doped with upconversion luminescence agent," *Catalysis Communications*, vol. 13, no. 1, pp. 31–34, 2011.

[19] L. Zhang, Y. Man, and Y. Zhu, "Effects of Mo replacement on the structure and visible-light-induced photocatalytic performances of Bi_2WO_6 photocatalyst," *ACS Catalysis*, vol. 1, no. 8, pp. 841–848, 2011.

[20] L. Zhang, H. Wang, Z. Chen, P. K. Wong, and J. Liu, "Bi_2WO_6 micro/nano-structures: synthesis, modifications and visible-light-driven photocatalytic applications," *Applied Catalysis B*, vol. 106, no. 1-2, pp. 1–13, 2011.

[21] Y. J. Chen, Y. Q. Zhang, C. Liu, A. M. Lu, and W. H. Zhang, "Photodegradation of malachite green by nanostructured Bi_2WO_6 visible light-induced photocatalyst," *International Journal of Photoenergy*, vol. 2012, Article ID 510158, 6 pages, 2012.

[22] J. Yu, J. Xiong, B. Cheng, Y. Yu, and J. Wang, "Hydrothermal preparation and visible-light photocatalytic activity of Bi_2WO_6 powders," *Journal of Solid State Chemistry*, vol. 178, no. 6, pp. 1968–1972, 2005.

[23] J. Wu, F. Duan, Y. Zheng, and Y. Xie, "Synthesis of Bi_2WO_6 nanoplate-built hierarchical nest-like structures with visible-light-induced photocatalytic activity," *Journal of Physical Chemistry C*, vol. 111, no. 34, pp. 12866–12871, 2007.

[24] S. Liu and J. Yu, "Cooperative self-construction and enhanced optical absorption of nanoplates-assembled hierarchical Bi_2WO_6 flowers," *Journal of Solid State Chemistry*, vol. 181, no. 5, pp. 1048–1055, 2008.

[25] B. Cheng, W. G. Wang, L. Shi, J. Zhang, J. R. Ran, and H. G. Yu, "One-pot template-free hydrothermal synthesis of monoclinic $BiVO_4$ hollow microspheres and their enhanced visible-light photocatalytic activity," *International Journal of Photoenergy*, vol. 2012, Article ID 797968, 10 pages, 2012.

[26] D. Wu, H. Zhu, C. Zhang, and L. Chen, "Novel synthesis of bismuth tungstate hollow nanospheres in water-ethanol mixed solvent," *Chemical Communications*, vol. 46, no. 38, pp. 7250–7252, 2010.

[27] J. Xu, W. Wang, E. Gao, J. Ren, and L. Wang, "Bi_2WO_6/Cu^0: a novel coupled system with enhanced photocatalytic activity by Fenton-like synergistic effect," *Catalysis Communications*, vol. 12, no. 9, pp. 834–838, 2011.

[28] J. Ren, W. Wang, S. Sun, L. Zhang, and J. Chang, "Enhanced photocatalytic activity of Bi_2WO_6 loaded with Ag nanoparticles under visible light irradiation," *Applied Catalysis B*, vol. 92, no. 1-2, pp. 50–55, 2009.

[29] Y. Li, J. Liu, X. Huang, and J. Yu, "Carbon-modified Bi_2WO_6 nanostructures with improved photocatalytic activity under visible light," *Dalton Transactions*, vol. 39, no. 14, pp. 3420–3425, 2010.

[30] E. Gao, W. Wang, M. Shang, and J. Xu, "Synthesis and enhanced photocatalytic performance of graphene-Bi_2WO_6 composite," *Physical Chemistry Chemical Physics*, vol. 13, no. 7, pp. 2887–2893, 2011.

[31] S. Murcia López, M. C. Hidalgo, J. A. Navío, and G. Colón, "Novel Bi_2WO_6-TiO_2 heterostructures for rhodamine B degradation under sunlike irradiation," *Journal of Hazardous Materials*, vol. 185, no. 2-3, pp. 1425–1434, 2011.

[32] M. Shang, W. Wang, L. Zhang, S. Sun, L. Wang, and L. Zhou, "3D Bi_2WO_6/TiO_2 hierarchical heterostructure: controllable synthesis and enhanced visible photocatalytic degradation performances," *Journal of Physical Chemistry C*, vol. 113, no. 33, pp. 14727–14731, 2009.

[33] J. Zhang, Z. H. Huang, Y. Xu, and F. Y. Kang, "Sol-gel-hydrothermal synthesis of the heterostructured TiO_2/N-Bi_2WO_6 composite with high-visible-light- and ultraviolet-light-induced photocatalytic performances," *International Journal of Photoenergy*, vol. 2012, Article ID 469178, 12 pages, 2012.

[34] F. Duan, Y. Zheng, and M. Chen, "Flowerlike $PtCl_4/Bi_2WO_6$ composite photocatalyst with enhanced visible-light-induced photocatalytic activity," *Applied Surface Science*, vol. 257, no. 6, pp. 1972–1978, 2011.

[35] M. Ge, Y. Li, L. Liu, Z. Zhou, and W. Chen, "Bi_2O_3-Bi_2WO_6 composite microspheres: hydrothermal synthesis and photocatalytic performances," *Journal of Physical Chemistry C*, vol. 115, no. 13, pp. 5220–5225, 2011.

[36] H. G. Yu, R. Liu, X. F. Wang, P. Wang, and J. G. Yu, "Enhancedvisible-lightphotocatalyticactivity of Bi_2WO_6 nanoparticles by Ag_2O cocatalyst," *Applied Catalysis B*, vol. 111-112, pp. 326–333, 2012.

[37] Q. Zhang, X. Chen, Y. Zhou, G. Zhang, and S. H. Yu, "Synthesis of $ZnWO_4@MWO_4$ (M = Mn, Fe) core-shell nanorods with optical and antiferromagnetic property by oriented attachment mechanism," *Journal of Physical Chemistry C*, vol. 111, no. 10, pp. 3927–3933, 2007.

[38] P. Madhusudan, J. R. Ran, J. Zhang, J. G. Yu, and G. Liu, "Novel urea assisted hydrothermal synthesis of hierarchical $BiVO_4/Bi_2O_2CO_3$ nanocomposites with enhanced visible-light photocatalytic activity," *Applied Catalysis B*, vol. 110, pp. 286–295, 2011.

[39] J. Bi, L. Wu, Z. Li, Z. Ding, X. Wang, and X. Fu, "A facile microwave solvothermal process to synthesize $ZnWO_4$ nanoparticles," *Journal of Alloys and Compounds*, vol. 480, no. 2, pp. 684–688, 2009.

[40] Z. Zheng, Z. H. Ai, M. Wang, and L. Z. Zhang, "Doping iodine in CdS for pure hexagonal phase, narrower band gap, and enhanced photocatalytic activity," *Journal of Materials Research*, vol. 26, no. 5, pp. 710–719, 2011.

[41] L. Wu, J. Bi, Z. Li, X. Wang, and X. Fu, "Rapid preparation of Bi_2WO_6 photocatalyst with nanosheet morphology via microwave-assisted solvothermal synthesis," *Catalysis Today*, vol. 131, no. 1–4, pp. 15–20, 2008.

[42] X. Chang, J. Huang, C. Cheng et al., "Photocatalytic decomposition of 4-t-octylphenol over $NaBiO_3$ driven by visible light: catalytic kinetics and corrosion products characterization," *Journal of Hazardous Materials*, vol. 173, no. 1–3, pp. 765–772, 2010.

[43] Y. Guo, X. Yang, F. Ma et al., "Additive-free controllable fabrication of bismuth vanadates and their photocatalytic activity toward dye degradation," *Applied Surface Science*, vol. 256, no. 7, pp. 2215–2222, 2010.

[44] D. Wu, H. Zhu, C. Zhang, and L. Chen, "Novel synthesis of bismuth tungstate hollow nanospheres in water-ethanol mixed solvent," *Chemical Communications*, vol. 46, no. 38, pp. 7250–7252, 2010.

[45] L. Ge and J. Liu, "Efficient visible light-induced photocatalytic degradation of methyl orange by QDs sensitized CdS-Bi_2WO_6," *Applied Catalysis B*, vol. 105, no. 3-4, pp. 289–297, 2011.

[46] H. Fu, C. Pan, W. Yao, and Y. Zhu, "Visible-light-induced degradation of rhodamine B by nanosized Bi_2WO_6," *Journal of Physical Chemistry B*, vol. 109, no. 47, pp. 22432–22439, 2005.

[47] C. Zhang and Y. Zhu, "Synthesis of square Bi_2WO_6 nanoplates as high-activity visible-light-driven photocatalysts," *Chemistry of Materials*, vol. 17, no. 13, pp. 3537–3545, 2005.

[48] S. Zhang, C. Zhang, Y. Man, and Y. Zhu, "Visible-light-driven photocatalyst of Bi_2WO_6 nanoparticles prepared via amorphous complex precursor and photocatalytic properties," *Journal of Solid State Chemistry*, vol. 179, no. 1, pp. 62–69, 2006.

[49] C. Wen, L. Sun, J. M. Zhang, H. Deng, and P. Wang, "Effect of iodine-doping on photocatalytic activity of TiO_2 photocatalyst," *Chemical Journal of Chinese Universities*, vol. 27, no. 12, pp. 2408–2410, 2006.

[50] W. Su, Y. Zhang, Z. Li et al., "Multivalency iodine doped TiO_2: preparation, characterization, theoretical studies, and visible-light photocatalysis," *Langmuir*, vol. 24, no. 7, pp. 3422–3428, 2008.

[51] Z. Zhang, W. Wang, L. Wang, and S. Sun, "Enhancement of visible-light photocatalysis by coupling with narrow-band-gap semiconductor: a case study on Bi_2S_3/Bi_2WO_6," *Acs Applied Materials & Interfaces*, vol. 4, no. 2, pp. 593–597, 2012.